J Mater Sci (2009) 44:1572–1579
DOI 10.1007/s10853-009-3322-1

Evidence for a double doping regime in Nd:YAG nanopowders

Marco Giorgetti · Mario Berrettoni ·
Maria Luisa Saladino · Eugenio Caponetti

Received: 2 December 2008 / Accepted: 4 February 2009 /

Abstract Nanopowders of Yttrium Aluminium Garnet doped with neodymium (Nd:YAG) were investigated by X-Ray Absorption Fine Structure (XAFS) at the Nd L_{III} edge in the 1.3–20.8% doping range. XANES spectra appear similar in the full range of the Nd concentration. However, a significant decrease in the white line intensity of XANES is revealed as the quantity of Nd doping ions increases. Plotting the white line intensity as a function of Nd doping ions reveals two linear trends with two different slopes, identifying a threshold value where the neodymium concentration reaches 5 at.% This experimental finding provides support for the existence of a double doping regime in Nd:YAG nanopowders.

Introduction

The work done by Ikesue et al. [1, 2] in 1995 showed that the transparent polycrystalline Nd:YAG ceramics could constitute an alternative material to the solid state lasers [3, 4]. Extensive research has been conducted in this field from then on [5]. The new synthesis approach allowed researchers to overcome the intrinsic limitations of the well-known Czochralski method for the crystal growth. These limitations include: (i) the intrinsic Nd segregation coefficient for YAG which limits the maximum solubility in YAG to 1 at.% during single crystal growth; (ii) the growth of the Nd:YAG single crystal which takes about 3–4 weeks; and (iii) the difficulties involved in controlling the microstructure which cause non-uniformities and structural defects such as coring, faceting and inclusions [6–8]. One common aim of research for these materials is to produce transparent ceramic by Nd:YAG nanopowder sintering [9, 10]. Researchers followed different routes to synthesis, including spark plasma sintering [11, 12], gel combustion [13] and freeze-dried processes [14], whilst our group used the co-precipitation method [15–17]. These methods satisfy the criteria of good dispersion of the rare earth in the matrix and of enhancing the Nd doping level in the YAG material as much as possible to improve laser efficiency.

The solubility limit of Nd in the YAG phase limits the quantity of Nd doping ions. When one phase exceeds the solubility limit and a second phase precipitates, then the lattice parameter of the first phase should generally indicate the value correlated to the saturation limit. In fact, the phase stability of the Nd:YAG crystalline material is systematically inspected by analysis of the corresponding X-ray diffraction patterns [13, 16, 18]. From such experiments, it has emerged that the measured lattice parameter

Electronic supplementary material The online version of this article (doi:10.1007/s10853-009-3322-1) contains supplementary material, which is available to authorized users.

M. Giorgetti (✉) · M. Berrettoni
Department of Physical and Inorganic Chemistry,
University of Bologna and Unità di Ricerca INSTM di Bologna,
Viale del Risorgimento 4, 40136 Bologna, Italy
e-mail: marco.giorgetti@unibo.it

M. L. Saladino
Department of Physical Chemistry, University of Palermo
and Unità di Ricerca INSTM di Palermo,
Viale delle Scienze, Parco D'Orleans II pad. 17,
90128 Palermo, Italy

E. Caponetti
Centro Grandi Apparecchiature, University of Palermo,
Via F. Marini 14, 90128 Palermo, Italy

of the cubic garnet phase (YAG) increases, following a linear trend, as the neodymium content becomes greater, due to the insertion of the large Nd ion into the dodecahedral sites formerly occupied by the yttrium ion. This occurs up to a certain threshold, which indicates the solubility limit. The formation of other yttrium aluminium oxide phases (such as the hexagonal YAH, the monoclinic YAM or YAP) takes place after the threshold, which could be as high as 27 at.% [18]. As a consequence, the lattice parameter plot becomes useless, since its values belong to the YAG phase only. The objective of the present paper is to find an experimental parameter other than the lattice parameter. This parameter permits us to check the entire Nd:YAG material beyond the threshold value. In addition, it would be the representative of the overall (multiphase) Nd:YAG sample. Kaplan et al. explored the solubility limit of MgO in Al_2O_3 and that of La and Y in Aluminum Oxynitride using wavelength-dispersive spectroscopy (WDS) [19, 20].

This paper describes an X-ray Absorption Spectroscopy (XAS) [21, 22] study of Nd:YAG nanopowders at various Nd doping amounts, obtained by the co-precipitation method [16]. XAS can be used as an alternative technique because it investigates a bulk of material. It acts as a local structural probe for the entire sample and makes it possible to obtain the structural information on the Nd in Nd:YAG ceramics. The technique is sensitive to the short-range order (a few Angstroms around the selected atom) and can be applied to disordered, amorphous, crystalline materials [22–25] and to solutions [26] as well. The study, based on the combined analysis of the X-ray absorption threshold (XANES) and of the Extended X-ray Absorption Fine Structure (EXAFS) has established *white line* height, which is capable of unambiguously identifying a second doping regime for the Nd-doped YAG samples. Some XAS studies are available at the Yttrium K-edge on the basic garnet structure [27, 28].

Experimental

Nd:YAG preparation and characterisation

The preparation of Nd:YAG doped with several neodymium quantities (in 1–24 at.% range of nominal concentration) was performed using the co-precipitation method and successive calcination at 950 °C. The preparation method has been described in detail in the previous paper [16]. It is important to note that all samples were processed at the same temperature. This avoids any possible effect due to the temperature dependency of the solubility limit. The same cooling rate as well as the same sintering time was chosen, thus limiting diffusion of the dopants from the matrix grains, thereby achieving a homogeneous dispersion of the dopants in the samples [19]. XRD and TEM characterisation were performed and are described in reference [16] as well. The particle/crystallite size as a function of the doping level was checked by line broadening analysis of the peak profiles of XRD (Rietveld). It turned out that the mean particle size, about 35 nm, does not depend on the doping quantity [16].

An example of the TEM micrographs of the Nd:YAG nanopowder doped with 1.6 at.% is reported in Fig. 1. The micrograph was performed using a JEOL 2010 operating at an accelerating voltage of 200 kV. It shows that the particles are crystalline, and characterised by a rounded morphology, and that the orientation is random. It is possible to observe agglomerate particles whose average size is around 30–70 nm.

Chemical analysis

The elemental composition of compounds was determined by Energy Dispersive X-Ray Fluorescence analysis (EDXF), courtesy of Analisi Control Laboratory, Corridonia, Italy. The analysis was directly done on pellets of

Fig. 1 TEM micrograph of Nd:YAG nanopowders doped at 1.6 at.%. Electron Diffraction

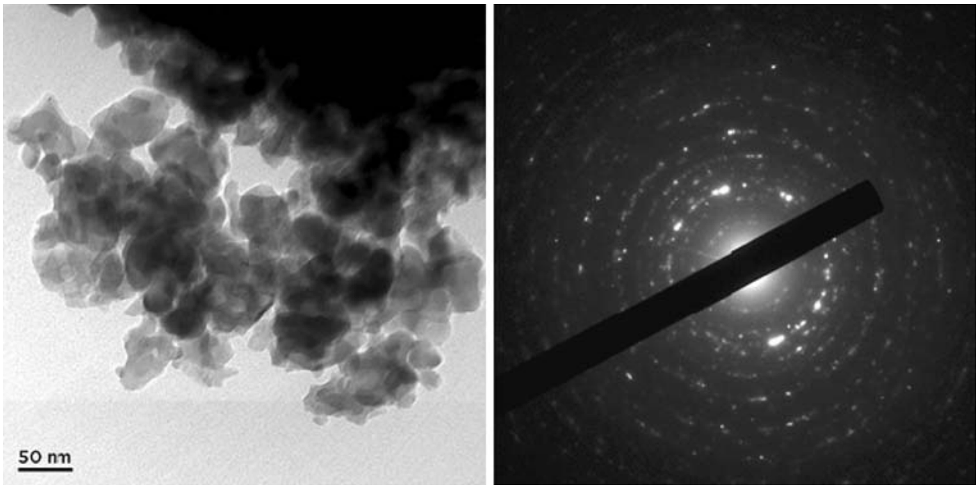

Table 1 List of the Nd:YAG samples (Nd at.%) investigated and actual composition as measured by EDXF

Compounds	Nd at.% nominal	Nd at.% EDXF	Garnet phase (%) by XRD analysis [9]
S1	1.6	1.3	99%
S2	3.2	2.4	97%
S3	6.4	4.9	96%
S4	12.8	13.1	90%
S5	24	20.8	75%

Garnet phase (%) obtained by Rietveld XRD analysis [9]

powdered samples. The results of the chemical analysis are reported in Table 1.

XAS data collection

Nd:YAG nanopowders mixed with boron nitride were pressed into pellets (3 tons). XAS experiments were performed at the Synchrotron Radiation Source (SRS) at Daresbury Laboratory, Warrington, England using the beam line 7.1. The storage ring operates at 1.6 GeV and a typical current of 240 mA. Internal references were used for Nd at each scan for energy calibration. This allows continuous monitoring of the energy during consecutive scans. No energy drifts of the monochromator were observed during the experiments. Data were acquired in the fluorescence mode using a Ge high-purity, 13-element solid state detector. The ionisation chamber was filled with an Ar/He gas mixture before sampling. Harmonics were rejected by detuning (80%). XAS spectra were collected at the L_{III} edge of neodymium from 200 eV before the edge up to $k = 12$ every 0.04 k with an integration time from 3 to 8 s, to obtain good quality data at high values of k.

XAS data analysis

XANES spectra were normalised to an edge jump of unity taking into account the atomic background after the edge as it comes out of the EXAFS analysis. Prior removal of the background absorption was done by subtracting a linear function extrapolated from the pre-edge region. The EXAFS analysis has been performed using the GNXAS package [29, 30] which takes the Multiple Scattering (MS) theory into account. The method is based on the decomposition of the EXAFS signals into a sum of several contributions, the n-body terms. It allows the direct comparison of the raw experimental data with a model theoretical signal. The procedure avoids any filtering of the data and enables a statistical analysis of the results. The theoretical signal is calculated ab initio and contains the relevant two-body $\gamma^{(2)}$ and the three-body $\gamma^{(3)}$ multiple scattering (MS) terms. The contribution from four-body $\gamma^{(4)}$ terms [31, 32] was checked out, but it was found to be negligible. The two-body terms associated with pairs of atoms probe their distances and variances. The three-body terms associated with triplets of atoms, probe angles, bond–bond and bond angle correlations. If useful, a single effective MS signal $\eta^{(3)}$ that includes both $\gamma^{(2)}$ and the $\gamma^{(3)}$ contributions can be used for the shells beyond the second one using the same three-atom coordinates both for the two-atom and for the three-atom contributions. The full definition of the parameters associated with the triplet of atoms has been reported elsewhere [29]. Data analysis was performed by minimising a χ^2-like function which compares the theoretical model to the experimental signal.

The phase shifts for the photoabsorber and backscatterer atoms were calculated ab initio starting from the structural model reported in the paper by Dobrzycki et al. [33]. They were calculated according to the muffin-tin approximation. The Hedin–Lundqvist complex potential [34] was used for the exchange-correlation potential of the excited state. Thereafter in the analysis, the starting signals were successively recalculated to account for any important structural variation from the starting model. The corresponding theoretical signal was recalculated before being used in the fitting procedure when a deviation of more than that of 10% of a selected structural parameter (atomic distance, angle, etc.) occurred with respect to the structural model. The effect of the existence of double electron transition on the EXAFS L_{III} edge of neodymium [35] was checked out, and it was found to be negligible in the present application due to the intrinsic noise of the measurements. In particular, the insertion of the $2p4d \rightarrow 5d^2$ double electron transition [35] does not improve the data analysis at all (the fit outcome is actually slightly worse) in the following fitting procedure, leading to the same structural parameters.

With reference to Table 2, we have included in the fitting procedures the following two-atom contributions: $\gamma_1^{(2)}$ Nd–O and $\gamma_2^{(2)}$ Nd–O with a degeneracy of 4, $\gamma_3^{(2)}$ Nd–Al, $\gamma_4^{(2)}$ Nd–Al, $\gamma_5^{(2)}$ Nd–Al and $\gamma_6^{(2)}$ Nd–Y with a degeneracy of 2. The core hole lifetime, Γ_c, was fixed to the tabulated value [36] and was included in the phase shift calculation. The experimental resolution used in the fitting analysis was about 2 eV, in agreement with the stated value for the beamline used.

The value of the amplitude reduction factor, S_0^2, was found to be 0.78(8) for the Nd L_{III} edge in good agreement with those quoted in the similar samples [37]. The relevant E_0 values, reported in Table 3, are displaced by several electronvolts with respect to the edge inflection point.

The overall number of floating parameters included in the fitting procedure was limited to nine: two bond distances, two EXAFS Debye–Waller factors, two coordination numbers and three non-structural terms: E_0, S_0^2

Table 2 Bond length and coordination numbers for YAG, YAH and YAM structures (data from the ICSD literature)

YAG			YAH			YAM		
Atoms	Distance (Å)	CN	Atoms	Distance (Å)	CN	Atoms	Distance (Å)	CN
Y–O	2.30	4	Y–O	2.27	6	Y–O	2.21	2
							2.25	1
							2.31	1
							2.36	1
Y–O	2.43	4	Y–O	2.63	2	Y–O	2.59	1
							2.65	1
Y–Al	2.99	2	Y–Al	3.38	6	Y–Al	3.18	1
	3.35	2					3.23	2
	3.67	2					3.50	1
							3.58	2
Y–Y	3.67	2	Y–Y	3.68	6	Y–Y	3.54	2
							3.63	1
							3.70	2
							3.86	1
							3.91	1

Table 3 EXAFS best-fitting results of Nd-doped YAG materials

Parameters	S1	S2	S3	S4	S5
Nd–O (Å)	2.35(2)	2.35(3)	2.35(3)	2.33(3)	2.28(4)
σ^2 (Å^2)	0.010(6)	0.011(6)	0.014(7)	0.015(7)	0.015(7)
CN 1	4.0(8)	4.0(8)	4.0(9)	3.3(9)	3.0(8)
Nd–O (Å)	2.48(4)	2.45(4)	2.46(3)	2.45(4)	2.44(3)
σ^2 (Å^2)	0.005(2)	0.005(2)	0.006(2)	0.006(2)	0.005(2)
CN 2	4.0(8)	4.0(8)	4.0(8)	4.0(9)	3.7(8)
Nd–Al (Å) [degeneracy = 2]	Fix	Fix	2.99(3)	Fix	Fix
σ^2 (Å^2)	Fix	Fix	0.024(9)	Fix	Fix
Nd–Al (Å) [degeneracy = 2]	Fix	Fix	3.41(3)	Fix	Fix
σ^2 (Å^2)	Fix	Fix	0.006(2)	Fix	Fix
Nd–Al (Å) [degeneracy = 2]	Fix	Fix	3.73(4)	Fix	Fix
σ^2 (Å^2)	Fix	Fix	0.006(3)	Fix	Fix
Nd–Y (Å) [degeneracy = 2]	Fix	Fix	3.80(4)	Fix	Fix
σ^2 (Å^2)	Fix	Fix	0.010(5)	Fix	Fix
S_0^2	0.78(8)	0.78(8)	0.78(8)	0.78(8)	0.78(8)
E_0 (eV)	6214(1)	6214(1)	6215(1)	6216(1)	6218(1)

The estimated parameter errors are indicated in parentheses

and the experimental resolution. This number of fitting parameters does not exceed the estimated 'number of independent data points, $N_{\mathrm{ind}} = (2\delta k\delta R/\pi) + 2 = 23$, where, $\delta k = 7.5$ and $\delta R = 4.5$, thus confirming the reliability of the minimisation.

The effect of the nanophase particle average size on XAS measurements [38] was considered. In this study, the average size of about 30–70 nm of the rounded Nd:YAG nanoparticles is large enough to avoid any grain boundary effects which produce the well-known effect of reducing the average coordination numbers. This effect is reported to be non-negligible only in relation to particles of average diameters of a few nanometers range [39, 40].

Results and discussion

Figure 2 shows the behaviour of the lattice parameter as a function of neodymium doping quantities relating to the samples investigated [16], as obtained by XRD analysis.

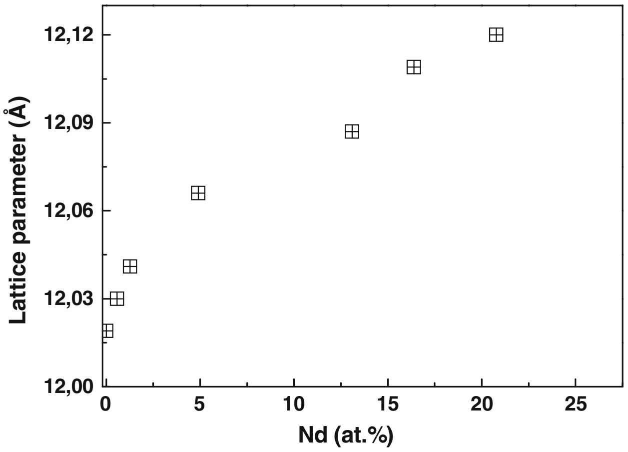

Fig. 2 Lattice parameter behaviour of the YAG phase as a function of neodymium content

The quantitative analysis of nanopowders obtained using the Rietveld method is reported in Table 1. The linear incremental behaviour of the lattice parameter up to about 5 at.% reflects the occurrence of Nd/Y atomic substitution in the YAG lattice due to the larger ionic radius of the doping ions ($\mathrm{Nd}^{3+}_{\mathrm{VIII}} = 1.12$ Å) compared to the host ion ($\mathrm{Y}^{3+}_{\mathrm{VIII}} = 1.01$ Å). In a different study [18], based on the micro-pulling method for the growth of Nd:YAG crystals, the linear behaviour was found to have been extended up to 27 at.%. These two examples reflect the heavy dependence of Nd solubility in the YAG phase on the method of preparation. After the liner behaviour, the observed trend of the data in Fig. 2 is no longer linear. It is well-known that an excess of doping ions can introduce possible defects in the YAG structure and it may promote the competitive formation of other crystalline phases above the solubility limit. As a matter of fact, authors generally postulate the concomitant formation of other phases, i.e., hexagonal YAH and perovskite YAM, and the curve is generally not considered after the threshold.

The use of the XAFS technique permits us to focus on the local atomic arrangement of the neodymium sites, providing electronic and structural information in the full range of the neodymium concentration. In this context, the XAFS analysis acts as a complementary structural probe of the XRD, where modifications of the cell parameter were limited to the YAG phase only, i.e., the predominant phase. Figure 3 shows the comparison of the normalised XANES curves of the investigated samples, recorded at the Nd $\mathrm{L}_{\mathrm{III}}$ edge. The curves are mainly characterised by a single threshold resonance line (the *white line*) followed by some other features. The similar shape of all the curves does not reveal any large difference in the neodymium atomic environment. However, a significant decrease in white line intensity is detectable as the amount of the Nd doping ion increases. The $\mathrm{L}_{\mathrm{III}}$ XANES spectra of lanthanides exhibits a single white line at a threshold which is due to a resonance from the $2p_{3/2}$ core level to vacant d states of the absorbing atom [41] modified by a local density of the unoccupied states. It is reported that white line intensity is related not only to the coordination environment of the photoabsorber but it also depends on the final state probed by the photoelectron, the electronic configuration of the absorbing atom and the type of neighbouring atoms [42]. Although a full explanation of this feature is beyond the scope of the present work, the dependence of white line intensity on the neodymium doping level is of particular interest. In fact, the progressive decrease in white line *intensity* as a function of neodymium content follows two distinctive regimes, as a close inspection of Fig. 4 reveals:

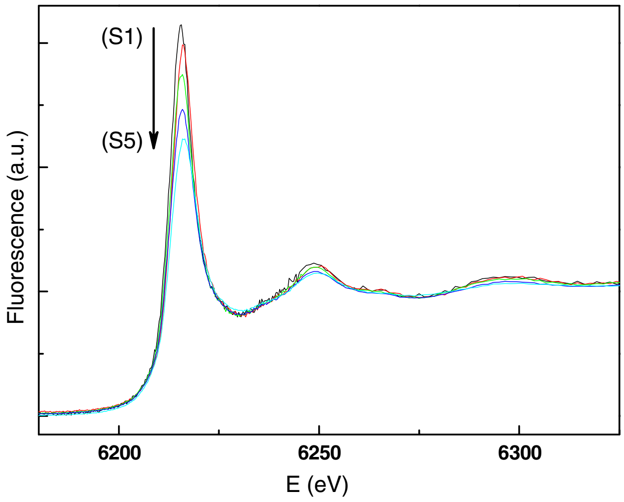

Fig. 3 Normalized XANES spectra recorded at the Nd $\mathrm{L}_{\mathrm{III}}$ edge of the compounds studied. Measurements were taken using fluorescence detection

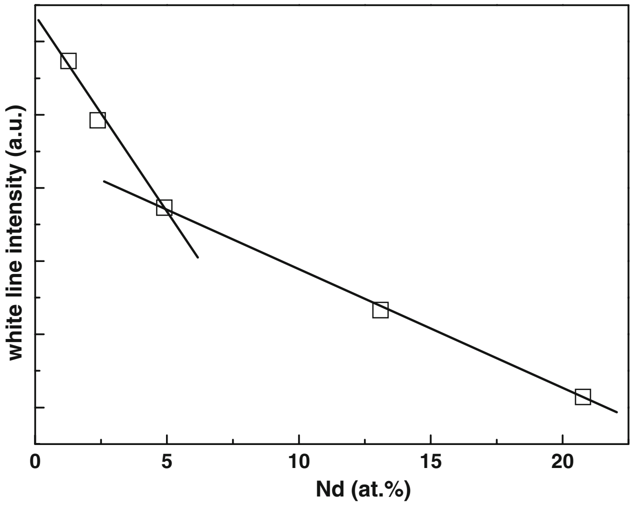

Fig. 4 Behaviour of the *white line intensity* of the XANES spectra recorded at the Nd $\mathrm{L}_{\mathrm{III}}$ edge as a function of neodymium content

two almost linear straight lines connect the experimental points, with a crossover at the neodymium concentration of about 5 at.%. This self-evident fact suggests the occurrence of the YAG phase up to 5 at.% and finds confirmation in the XRD data listed in Table 2 (the quantity of the YAG phase is around 100 at.% up to 5 at.%). Moreover, the second linear trend with a different slope underlines the fact that all the material probed is subject to structural and electronic modifications. These experimental findings may be explained as follows. Nd doping is possible without foreign phases up to 5%. Consequently, only garnet phase is found using XRD, and the lattice constant, the lattice parameter and white line intensity change almost linearly with a constant slope. Between 5 and 20 at.% Nd doping (sample S5) garnet phase is still present, as observed from the lattice parameter in Fig. 2 which still changes, but additionally, other Nd-bearing phases occur (see Table 1). Because the XANES spectra are the result of a superposition of Nd within garnet and Nd within other phases (YAM and YAH), this explains the difference in the slope, starting at the point where these foreign phases first appear.

Table 2 lists the relevant bond lengths and corresponding coordination numbers related to the Y site in the YAG, YAH and YAM phases from the literature. In view of the Y/Nd substitution, the table also indicates the atomic neighbours of the Nd atom which may be probed in an EXAFS experiment. The table makes clear the differences in the first shell of the Y (Nd) in the three phases involved: Nd is eightfold coordinated in YAG; a perfect octahedron in the YAH plus two additional oxygens at longer distance and a very distorted pseudo-octahedron in the YAM phase. Therefore, YAH and YAM phases are characterised by lower first shell coordination numbers. Moreover, the outer shells of atoms appear very similar.

Of course, a rigorous EXAFS analysis would include the second phases on the level of 10 and 25 at.% in samples S4 and S5, respectively (see Table 1). The literature reports some examples of EXAFS analysis performed for two different arrangements of neighbours near the photoabsorber [43, 44]. Here, the EXAFS data would only support the XANES spectra behaviour and hence, it was decided to simplify the approach to the EXAFS data analysis: (1) the structural model needed for the calculation was the one which appears in reference [34], and which is indicated in Table 2; (2) EXAFS data analysis was focused on the first shell contributions after an optimisation procedure; (3) optimisation of the various parameters was done on sample S3, since it represents the highest doped sample exclusively with the YAG phase; (4) the structural contributions of the outer shells, from aluminium and yttrium atoms, were constrained to the values optimised in sample S3; (5) the contribution from Nd to Nd interaction was checked out but its inclusion did not improve data analysis and hence was not considered at all.

Figure 5 shows the best fit results for sample S5: panel (a) displays the comparison of the theoretical and experimental EXAFS signals; the corresponding FT's signals are shown in panel (b). In both cases, the theoretical curves match well with the experimental ones. The inter-atomic distances and the corresponding EXAFS Debye–Waller factors of the samples investigated are shown in Table 3. The errors associated with the parameters obtained with the EXAFS analysis are indicated as well. The latter were determined by correlation maps [45] (contour plots) for each pair of highly correlated parameters. Figure 6 shows the contour plots for compound S1 and S5, as an example. These plots were selected amongst the parameters with a strong correlation to reflect the highest error. The estimated statistical error is associated with the 95% confidence interval. The relative errors associated with the L_{III} edge appear larger than those normally quoted for the *K*

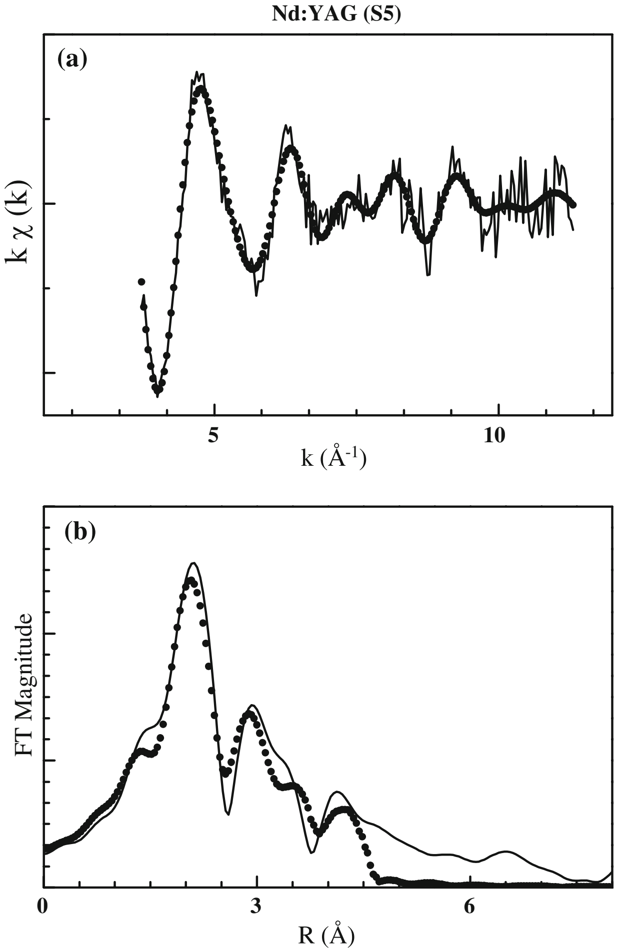

Fig. 5 Comparison of the experimental (-) and theoretical (…) *k*-weighted EXAFS signals for compounds S5 at the Nd L_{III} edge (Panel a); Corresponding FT signals are shown in panel (b)

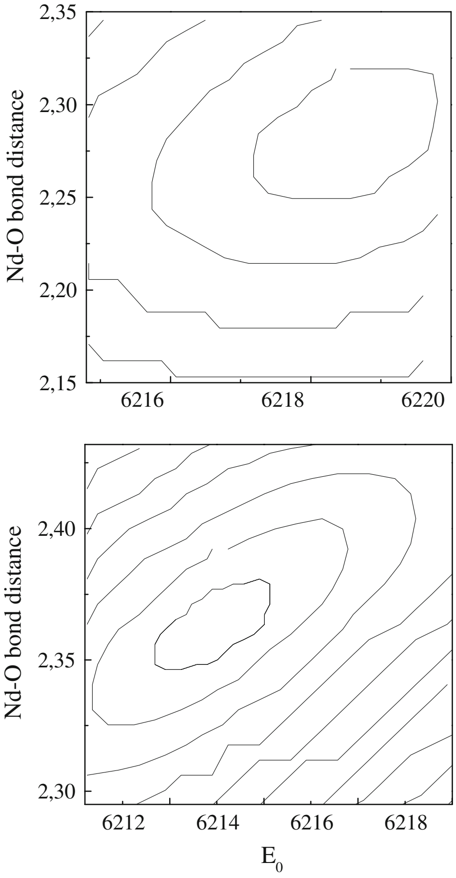

Fig. 6 Examples of the two dimensional section of the parameter space (contour plots). Nd–O first shell distance and the E_0 variable for the compound S5 (up) and S1 (down). The inner elliptical contour corresponds to the 95% confidence level

threshold as a consequence of the limited *k* range available for the analysis [46].

The Nd–O first shell distance in sample S1 is longer than that corresponding to Y–O in the crystalline YAG, reflecting the larger ionic radius of Nd ions compared to Y ions. Moreover, Nd–O first shell distances slightly decrease upon increasing the Nd doping level, as they are 2.35 and 2.48 Å in sample S1, but become 2.28 and 2.44 Å, respectively, in sample S5. The Nd–O bond length quotation agrees with the Nd–O first shell distance found in similar chemical environments (Nd oxides [47] and Nd phosphate glasses [35]). In addition, the EXAFS Debye–Waller factors are seen to be constant in the entire set of samples and are consistent with those available in the literature for similar Nd environments [35]. Here, the specific structural parameter, which plays a key role, is the value of the coordination number of the first shell, which may be described as CN = CN1 + CN2. As Table 2 reveals, the total CN decreases progressively after sample S3: the total CN varies from eight in samples S1–S2–S3 to about 6.7 in sample S5. In spite of the intrinsic difficulties involved in determining coordination numbers with EXAFS, its value decreases as the Nd level becomes higher. This behaviour can be explained by assuming the occurrence of YAH and YAM phases in addition to the YAG one in samples with a high neodymium concentration. As we have already pointed out, YAH and YAM phases are characterised by a lower first shell coordination number compared to the YAG one. Indeed, based on a simple calculation, and taking into consideration the data in Tables 1 and 2, the sample S5 should have an Nd–O coordination number of about seven, which is close to that observed using the EXAFS analysis.

Conclusions

The white line intensity of the Nd L_{III} edge XAS spectra was used as an indicator of different Nd-bearing phases that occurs in Nd-doped YAG nanopowder samples. Plotting white line intensity as a function of Nd doping ion revealed two well-defined linear trends, defined in the 0–5 at.% and 5–21 at.% Nd concentration ranges. The EXAFS analysis of the first shell shows Nd–O distances shortening, and the corresponding coordination number decreases, as the Nd doping level increases. These structural characteristics provide support for a double doping regime of the Nd-doped YAG samples, further indicating the concomitant formation of YAH and YAM phases in samples where the concentration of neodymium exceeds 5 at.%. This paper presents an approach which is complementary to the cell parameter measurements obtained using XRD because it makes it possible to extend the range of investigation over the solubility limit of the Nd in the YAG phase, and additional other Nds within other phases occur.

Acknowledgements The authors would like to thank MIUR for supporting this research through the PRIN 2007 prot. 20077 R3PXF_002 “New nanocomposite preparation for optical, electric and magnetic applications.” TEM experimental data were provided by Centro Grandi Apparecchiature—UniNetLab—Università di Palermo funded by P.O.R. Sicilia 2000–2006, Misura 3.15 Azione C Quota Regionale. XAS measurements at Daresbury Laboratory were funded by the European Community—Research Infrastructure Action under the FP6 “Structuring the European Research Area” Programme (through the Integrated Infrastructure Initiative “Integrating Activity on Synchrotron and Free Electron Laser Science”). Thanks are due to S. Fiddy (Daresbury Laboratory) for his help in the execution of the measurements.

References

1. Ikesue A, Furusato I, Kamata K (1995) J Am Ceram Soc 78:225
2. Ikesue A, Kinoshita T, Kamata K, Yoshida K (1995) J Am Ceram Soc 78:1033
3. Ahmed MA, Khalil AAI, Solyman S (2007) J Mater Sci 42:4098. doi:10.1007/s10853-006-1151-z

4. Xu WL, Yue TM, Man HC (2008) J Mater Sci 43:942. doi: 10.1007/s10853-007-2208-3
5. Ikesue A, Aung Y, Taira T, Kamimura K, Yoshida K, Missing GA (2006) Ann Rev Mater Res 36:397
6. Cockayne B (1966) J Am Ceram Soc 49:204
7. Brandle CD, Barns LR (1974) J Cryst Growth 26:169
8. Caslavsky JL, Viechnicky JD (1980) J Mater Sci 15:1709. doi: 10.1007/BF00550589
9. Lee SH, Kochawattana S, Messine GL, Dumm JQ, Quarles G, Castello V (2006) J Am Ceram Soc 89:1945
10. Vaidhyanathan B, Binner JGP (2006) J Mater Sci 41:5954. doi: 10.1007/s10853-006-0260-z
11. Chaim R, Shen ZJ (2008) J Mater Sci 43:5023. doi:10.1007/s10853-008-2742-7
12. Chaim R (2006) J Mater Sci 41:7862. doi:10.1007/s10853-006-0605-7
13. Li J, Pan Y, Qiu F, Wu Y, Liu W, Guo Y (2007) Ceram Int 33:1047
14. Rabonovitch Y, Bogicevic C, Karolak F, Tetard D, Dammak H (2008) J Mater Process Technol 199:314
15. Caponetti E, Enzo S, Lasio B, Saladino ML (2007) Opt Mater 29:1240
16. Caponetti E, Saladino ML, Serra F, Enzo S (2007) J Mater Sci 42:4418. doi:10.1007/s10853-006-0660-0
17. Caponetti E, Chillura Martino D, Saladino ML, Leonelli C (2007) Langmuir 23:3947
18. Lipinska L, Lojko L, Klos A, Ganschow S, Diduszko R, Ryba-Romanowski W, Pajaczkowska A (2007) J Alloys Compd 432:177
19. Miller L, Avishai A, Kaplan WD (2006) J Am Ceram Soc 89:350
20. Miller L, Kaplan WD (2008) J Am Ceram Soc 91:1693
21. Rehr JJ, Albers RC (2000) Rev Mod Phys 72:621
22. Filipponi A (2001) J Phys Condens Matter 13:R23
23. Giorgetti M, Berrettoni M, Scaccia S, Passerini S (2006) Inorg Chem 45:2750
24. Giorgetti M, Passerini S, Smyrl WH, Berrettoni M (1999) Chem Mater 11:2257
25. Giorgetti M, Berrettoni M, Smyrl WH (2007) Chem Mater 19:5991
26. D'Angelo P, Benfatto M, Della Longa S, Pavel NV (2002) Phys Rev B 66:064209
27. Gautier N, Gervais M, Landron C, Massiot D, Coutures JP (1998) Phys Stat Sol A 165:329
28. Landron C, Hennet L, Coutures JP, Gailhanou M, Gamond M, Berar JF (1998) Europhys Lett 44:429
29. Filipponi A, Di Cicco A, Natoli CR (1995) Phys Rev B 52:15122
30. Filipponi A, Di Cicco A (1995) Phys Rev B 52:15135
31. Giorgetti M, Berrettoni M, Filipponi A, Kulesza PJ, Marassi R (1997) Chem Phys Lett 275:108
32. Giorgetti M, Berrettoni M (2008) Inorg Chem 47:6001
33. Dobrzycki L, Bulska E, Pawlak DA, Frukacz Z, Wozniak K (2004) Inorg Chem 43:7656
34. Hedin L, Lundqvist BI (1971) J Phys C 4:2064
35. Solera JA, Garcia J, Proietti MG (1995) Phys Rev B 51:2678
36. Krause M, Oliver JH (1979) J Phys Chem Ref Data 8:329
37. Karabulut M, Marasinghe GK, Metwalli E, Wittenauer AK, Brow RK (2002) Phys Rev B 65:104206
38. Stern EA, Siegel RW, Newville M, Sanders PG, Haskel D (1995) Phys Rev Lett 75:3874
39. Witkowska A, Di Cicco A, Principi E (2007) Phys Rev B 76:104110
40. Frenkel AI, Hills CW, Nuzzo RG (2001) J Phys Chem B 105:12689
41. Bianconi A, Marcelli A, Dexpert H, Karnak R, Totani A, Jo T, Petiau J (1987) Phys Rev B 35:806
42. Wu Z, Benfatto M, Natoli CR (1998) Phys Rev B 57:10336
43. Bacewicz R, Twaròg A, Malinowska A, Wojtowicz T, Liu X, Furdyna JK (2005) J Phys Chem Solids 66:2004
44. Klepka MT, Nedelko N, Greneche JM, Lawniczak-Jablonska K, Demchenko IN, Slawinska-Waniewska A, Rodrigues CA, Debrassi A, Bordini C (2008) Biomacromolecules 9:1586
45. Filipponi A (1995) J Phys Condens Matter 7:9343
46. D'Angelo P, De Panfilis S, Filipponi A, Persson I (2008) Chem Eur J 14:3045
47. Nitani H, Nakagawa T, Yamanouchi M, Osuli T, Yuja M, Yamamoto TA (2004) Mater Lett 58:2076